Research papers

Entry pressure for the rough capillary: Semi-analytical model, Lattice Boltzmann simulation

Bei Wei[a], Jian Hou[a,b,*], Haibo Huang[c], Michael C. Sukop[d], Yongge Liu[a], Kang Zhou[a]

[a] School of Petroleum Engineering, China University of Petroleum, Qingdao, Shandong 266580, China
[b] State Key Laboratory of Heavy Oil Processing, China University of Petroleum, Qingdao, Shandong 266580, China
[c] Department of Modern Mechanics, University of Science and Technology of China, Hefei, Anhui 230026, China
[d] Department of Earth and Environment, Florida International University, Miami, FL 33199, USA

ABSTRACT

We develop a semi-analytical model to calculate the entry pressure in rough capillaries based on an energy balance principle and wetting theory on rough surfaces. During the drainage process, we assume fluids form arc menisci at corners of capillary cross-sections depending on the apparent angle, and that there is a wetting phase film adsorbed on the rough surface depending on the wetting condition. A Logistic model is proposed to explain the contact angle dependence on the structure of rough surfaces. Then the capillary entry pressure is calculated by extended MS-P (Mayer, Stowe and Princen) method. We verify the model using the pseudopotential Lattice Boltzmann model and obtain good agreement between the analytical and simulated pressures. Taking capillaries with triangular sections with pillar pillar-type rough surfaces as example, we discuss how rough structures and contact angles influence capillary behaviors. The results reveal that both the wetting phase saturation and entry pressure of rough capillaries are larger than those in smooth capillaries under the same conditions. Moreover, the entry pressure is not sensitive to the roughness factor under strong wetting conditions and is much more sensitive to the pillar asperity height than the other structure parameters.

1. Introduction

The phenomena of flow through porous media are ubiquitous in nature and artificial materials. Some examples include the oil flow underground, microcirculation of blood in animals and gas migration in packed bed. The pore scale ranges from nanometers to micrometers in porous media, such as tight sandstone and shale, which requires researchers to pay more attention to pore scale flow to further reveal flow mechanisms.

The shape of the pore space in porous media is irregular and the connectivity is complex. Also, the flow often involves multiple fluids. One popular tool used to model multi-phase flow at pore scale is pore-network modeling, where the porous medium is described as a network of pores connected by capillaries using an idealized geometry (Blunt et al., 2002) that in the simplest case are considered either completely full or completely empty depending on the capillary pressure. However, there will always be some fluid remaining in the corners both after drainage (a non-wetting fluid displaces a wetting fluid) and imbibition (a wetting fluid displaces a non-wetting fluid) processes. So pores or throats in such networks are usually assumed to have angular cross-sectional shapes, such as triangle, square, and star, to hold the fluid

phase in a mathematically tractable way. We focus on a quasi-static primary drainage process controlled by capillary pressure in the following discussion, i.e., the flow rate is very low and the capillary number is small (Hanspal et al., 2013).

No matter whether in experiments or simulations, capillary behavior is the basis for getting the capillary pressure curve and the relative permeability curve (Zhang and Yu, 2016; Ye et al., 2017). An important property of capillary behavior is the value of the capillary entry pressure (or threshold pressure), i.e., the minimum pressure difference required for the non-wetting fluid to penetrate a capillary filled with a wetting fluid. The most popular theoretical model to calculate the capillary entry pressure is the so-called MS-P method, which was originally proposed by Mayer and Stowe (1965) and further developed by Princen (1969a,b, 1970). Based on the MS-P method, Oren et al. (1998) derived the threshold pressures of triangular tubes under different flow conditions (Oren and Bakke, 1998) and Lago et al. (2001) derived the threshold pressure in a capillary with a polygonal cross-section (Lago and Araujo, 2001).

However, most of the works ignore pore surface roughness in pore scale modeling, though it influences the contact angle and contact angle hysteresis significantly (Hecht et al.,2013, Mortazavi et al., 2013), as
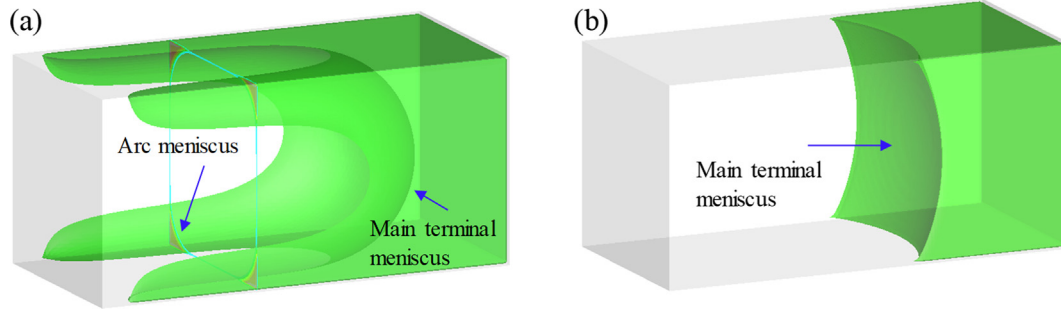
Fig. 1. Schematic of the liquid distributions when non-wetting fluid invades wetting fluid in a square capillary, the green color represents non-wetting fluid: (a) co-occurrence of AMs and MTM under strong wetting condition for wetting fluid (b) only MTM appears under poor wetting condition. (For interpretation of the references to color in this figure legend, the reader is referred to the web version of this article.)

well as affecting energy consumption due to interface contact between fluids and solids during flow. The surface roughness plays an important role in many flow processes, for example, with nanoparticles injection into porous media, particles would be adsorbed onto the surface driven by DLVO forces, forming a rough surface (Rao, 2010; Chowdhury et al., 2011). Consequently, both the contact angle and microstructure of the surface would change during the flow process. The influence of surface roughness on the apparent contact angle of the droplet is generally understood as lying between two theoretically extreme situations, i.e., the Cassie-Baxter (C-B) state and Wenzel state (Cassie, 1948; Wenzel, 1949; Whyman and Bormashenko, 2008). In the C-B state, the droplet remains suspended above the asperities in the surface. In the Wenzel state, the droplet fills the grooves between the roughness elements. Admittedly, these two classical models are not always accurate since they fail to capture the effect of many interactions occurring during wetting, such as the heterogeneity (Lundgren et al., 2007), hierarchical structure (Badge et al., 2013), and geometry of bumps or cavities on the surface (Afferrante and Carbone, 2014). In addition, the wetting state could change under certain conditions, for example, there would be a transition from Cassie to Wenzel state when the drop is acted on by an external force or the structure of the rough surface is modified (Guo et al., 2014). Thus, some more accurate state equations have been developed but mainly are extensions of these two models (Bormashenko, 2015). In this study, we also derive a new equation for the Wenzel wetting state and verify the model by Lattice Boltzmann (LB) simulation results. Rather than from physical mechanisms, we propose the new equation from the perspective of mathematical modeling using a Logistic model.

Extrand (2007) studied retention forces of a liquid slug in a rough capillary tube with symmetric or asymmetric features and the imbalance of capillary forces that leads to directionally biased wetting was examined. A model was described by Butt (2008) to calculate capillary forces between solid surfaces analytically using the Kelvin equation, in which roughness is considered with an asperity distribution function. There were also many other numerical methods reported to study capillary behavior in rough capillaries (Liu et al., 2007; Rostami and Streator, 2017); however, these methods are generally complex and do not offer straightforward linkages between capillary behavior and flow. As to the theory on capillary entry pressure considering rough surfaces, though Tsakiroglou and Payatakes add pore-wall roughness features to a network model using concepts from fractal geometry (Tsakiroglou and Payatakes, 1993), they did not give an analytical model to enable calculation of the capillary entry pressure exactly based on the microstructure of pore shapes.

In this work, we present a semi-analytical expression for the capillary entry pressure for the case of rough capillaries with polygonal cross-sections using the MS-P method, and verify the model using LB simulation. Capillary entry pressures in smooth capillaries are compared with those in rough capillaries. A study of the dependence of the capillary behavior on the shape factor, contact angle, groove width, and

asperity width and height is done for triangle shapes. The study is not only useful for revealing flow mechanisms at micro- and nano-scales, but also attractive for a variety of industry applications such as oil development, wastewater treatment, and MEMS-based fluidic devices.

2. Theory background

In this section, we will introduce MS-P method and its application to calculate capillary entry pressure in capillaries with polygonal cross-section.

2.1. MS-P method

Capillary forces prevent non-wetting fluid from spontaneously entering wetting fluid filled throats when the non-wetting fluid invades the wetting fluid in a non-circular capillary. Non-wetting fluid can only enter an available throat if the capillary pressure exceeds the threshold capillary pressure, at which point the wetting phase will be displaced from the central region leaving some residual in the corners. The invading meniscus is referred to as the main terminal meniscus (MTM), while the menisci formed in the cross-sectional plane are referred to as arc menisci (AMs) (Mason and Morrow, 1991). In the absence of gravity, the MS-P method for calculating the capillary entry pressures relies on equating the curvature of the AMs to that of the MTM. There is a critical contact angle for the occurrence of AMs in the corner. That is to say, only when the contact angle is smaller than the critical contact angle of the corner, can the MTM and AMs appears simultaneously. Fig. 1 shows a three dimensional example where non-wetting fluid invades wetting fluid in a square capillary, in which there is a co-occurrence of AMs and MTM in strong wetting conditions while there is no AM in poor wetting condition.

The capillary pressure P_c is calculated as follows:

$$P_c = P_n - P_w, \tag{1}$$

where the subscripts w and n refer to the wetting and non-wetting phases, respectively.

If the AMs are displaced a small distance dx, the work of the displacement must be balanced by the change in surface free energy,

$$P_c A_{eff} dx = (L_{nw}\gamma_{nw} + L_{ns}\gamma_{ns} - L_{ns}\gamma_{ws})dx, \tag{2}$$

where the subscript s indicates the solid, A_{eff} is the effective area occupied by the non-wetting phase, L_{ns} is the length of the solid wall in contact with the non-wetting phase, L_{nw} is the perimeter of the AMs, and γ is the interfacial tension. When the contact angle is θ, Young's equation yields the following:

$$\gamma_{ns} - \gamma_{ws} = \gamma_{nw}\cos\theta, \tag{3}$$

and the energy balance equation can be simplified as follows:
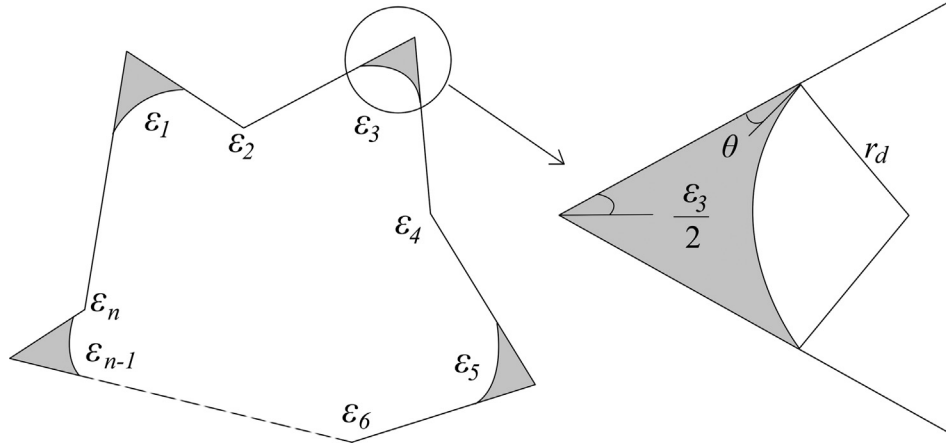
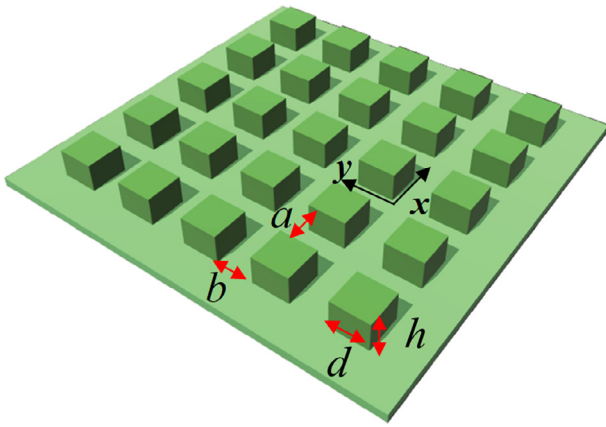Fig. 2. Arbitrary polygonal cross-section, the corner can be regarded as a wedge.

Fig. 3. Rough surface used in the model, and can be assembled to rough capillaries with different polygonal cross sections; y direction is the drainage direction.

$$\frac{P_c}{\gamma_{nw}} = \frac{L_{nw} + L_{ns}\cos\theta}{A_{eff}} = \frac{L_{eff}}{A_{eff}}. \tag{4}$$

If the radius of the threshold drainage curvature is r_d (threshold radius), the Young-Laplace equation yields the following:

$$P_c = \frac{\gamma_{nw}}{r_d}. \tag{5}$$

The capillary entry pressure and the threshold drainage radius are then obtained by solving Eqs. (4) and (5); the wetting phase saturation is calculated based on the geometrical characteristics of the cross-section.

2.2. Capillary entry pressures in smooth polygonal capillaries

Lago and Araujo (2001) studied the capillary entry pressure in capillaries with polygonal cross-section when the wettability of capillaries is uniform. During primary drainage, the threshold pressure is equal to the capillary pressure.

A cross-section of an arbitrary polygon is shown in Fig. 2, where the contact angle is θ, the corner angle is denoted by ε_i, and the drainage radius is r_d. With some geometric calculations, we can get:

$$L_{ns} = P - 2r_d \sum_1^n \left(\cos\theta\cot\left(\frac{\varepsilon_i}{2}\right) - \sin\theta\right)\delta_i, \tag{6}$$

$$L_{nw} = 2r_d \sum_{i=1}^n \left(\frac{\pi}{2} - \frac{\varepsilon_i}{2} - \theta\right)\delta_i, \tag{7}$$

$$A_{nw} = r_d^2 f_T, \tag{8}$$

where

$$\delta_i = \begin{cases} 0, & \varepsilon_i > \pi - 2\theta \\ 1, & \varepsilon_i \leqslant \pi - 2\theta \end{cases}, \tag{9}$$

$$f_T(n,\theta) = \sum_{i=1}^n \left[\cos\theta\left(\cos\theta\cot\left(\frac{\varepsilon_i}{2}\right) - \sin\theta\right) - \left(\frac{\pi}{2} - \frac{\varepsilon_i}{2} - \theta\right)\right]\delta_i. \tag{10}$$

Then the MS-P method gives:

$$f_T r_d^2 - P\cos\theta r_d + A = 0, \tag{11}$$

where f_T is an intermediate variable, A is the area of the polygon, p is the perimeter, γ refers to the interfacial tension between wetting phase and non-wetting phase, and δ_i is a dimensionless coefficient.

The wetting phase saturation can be calculated further as,

$$S_w = \frac{r_d^2 f_T}{A}. \tag{12}$$

3. Model description

3.1. Model assumption

The rough surface used in the model is homogeneous and the pillar of the surface is square, as shown in Fig. 3, in which a, b, d, and h are the groove width, groove length, asperity pillar width, and pillar height respectively. There are a few ways to measure the surface roughness parameters of real porous media, such as the experiment methods of scanning electron microscopy (SEM) (Quéré, 2008), field emission scanning electron microscopy (FE-SEM) (Monfared et al., 2015), 3D laser scanning(Hoła et al., 2015), and Atomic force microscopy (AFM) (Al-Anssari et al., 2016). For some regular arranged porous media, FEM or FE-SEM images can provide enough information to estimate the roughness parameters. While for irregular arranged porous media, 3D laser scanning (μm-mm) or AFM (nm-μm) images can help, depends on the pore scale. To construct an equivalent rough surface similar with Fig. 3, we need measure the average groove width, groove length, asperity pillar width, and pillar height of porous media surface. Obtaining the surface morphology surface by experiment methods stated above, the roughness parameters in different cross sections then could be calculated averagely.

The geometrical parameters that characterize the roughness are as follows (Chandra and Yang, 2011):
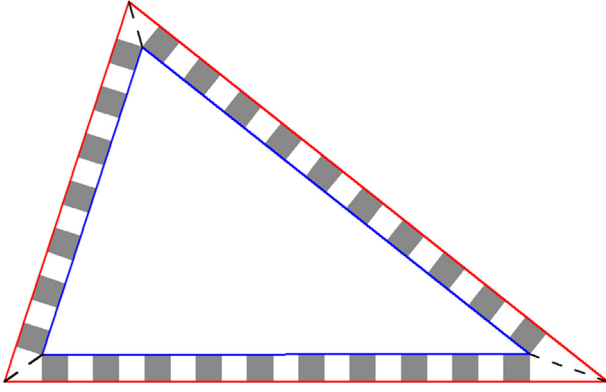
$$r_f = \frac{(d+a)(d+b) + 4dh}{(d+a)(d+b)}, \tag{13}$$

Fig. 4. Triangle cross-section with rough surface.

$$f_{lx} = \frac{d}{d+a}, \quad f_{ly} = \frac{d}{d+b}. \tag{14}$$

where r_f is the roughness factor, which is the ratio of actual surface area to its horizontal projection. f_{lx} and f_{ly} represent the ratio of the sum of asperity length to the side length along the groove in the x and y directions, respectively.

The underlying assumptions are that the drainage is along the y-axis direction and that the non-wetting phase would suspend above or fill in the grooves according to the wetting condition. In fact, the non-wetting phase usually stays in a transition state wherein the non-wetting phase only partly penetrates the grooves and there is a wetting fluid film on the base of grooves.

When the non-wetting phase begins to occupy the polygonal cross-section, the cross-section can be divided into two regions: the central region inside the shape and the border region including grooves and asperities. Taking the triangle as shown in Fig. 4 as an example, one region is the triangle inside the blue line, the other region is the area between the blue line and red line. In the central region, the corners still hold the wetting phase but depend on the apparent contact angle rather than Young's contact angle on the rough surface. Denote the film height of wetting phase in a groove as h_w. Then the wetting phase border region holds the can be described by h_w. The outlines of the two regions (the blue and red lines in Fig. 4) are two similar polygons; no matter the polygon is concave or convex. Denote the perimeter, area, and corner angle of the polygonal cross section (outer polygon) as P_0, A_0, and ε_i, and the perimeter and area of the central region (inner polygon) as P and A respectively. The similarity ratio of the inner polygon to the outer polygon k satisfies:

$$k = P/P_0 = (P_0 - 2\sum h\cot\frac{\varepsilon_i}{2})/P_0 \tag{15}$$

In addition, the model does not consider contact angle hysteresis, however readers can use the receding contact angle instead of the static contact angle if necessary, and we will also give some supplementary information on contact angle hysteresis based on Lattice Boltzmann simulation results.

3.2. Capillary entry pressures in the rough capillary

As shown in Fig. 5, in the rough capillary, the non-wetting phase mainly exists in the central region; the rest of the non-wetting phase fills the grooves of the border region except the corners. The triangle is just an example, and the model can be applied to all polygons.

We first calculate the effective area occupied by the non-wetting phase A_{eff} (i.e., A_{nw}) and the effective length L_{eff} (i.e., $L_{\mathrm{nw}} + L_{\mathrm{ns}}\cos\theta$) based on Fig. 6, because they are needed to obtain the entry pressure according to MS-P method in Eq. (4).

According to similarity principle, the inner polygon area and perimeter are,

$$P = kP_0, A = k^2 A_0. \tag{16}$$

The cross-sections in a rough capillary are not always like the structure shown in Fig. 5(b), and there are also some smooth cross-sections in one certain direction. That means that along the long axis of a pore perpendicular to these cross-sections, roughness of the pore walls will be present over some fraction of the total pore length and absent everywhere else, as shown in Fig. 6. In Fig. 6, L_{ns} can be divided to two parts, one part is the length of asperity tops and the other part is the immersed height of non-wetting fluid in grooves, so

$$L_{ns1} = \left[P - 2r_d \sum_1^n \left(\cos\theta^*\cot\left(\frac{\varepsilon_i}{2}\right) - \sin\theta^*\right)\delta_i\right] F(h_w) f_{ly}$$

$$= (P - 2r_d S_1) F(h_w) f_{ly}, \tag{17}$$

where $F(h_w) = \begin{cases} 1, & h_w = 0 \\ f_{lx} = \frac{d}{d+a}, & else \end{cases}$, $S_1 = \sum_1^n (\cos\theta^*\cot(\frac{\varepsilon_i}{2}) - \sin\theta^*)\delta$, and $(P - 2r_d S_1)$ is dashed line length in Fig. 6(b). As rough cross-sections and smooth cross-sections arrange alternately along the y-axis direction and the non-wetting phase only contacts the solid in rough ones, the length is multiplied by f_{ly} here to capture this feature. And the other part of L_{ns} is

$$L_{ns2} = 2(h - h_w)\frac{(P - 2r_d S_1)}{d+a} f_{ly}, \tag{18}$$

Then the total L_{ns} is the sum of these two parts,

$$L_{ns} = L_{ns1} + L_{ns2} = v(P - 2r_d S_1), \quad v = f_{ly}\left(F(h_w) + \frac{2(h - h_w)}{d+a}\right). \tag{19}$$

Similarly, L_{nw} includes the length of AMs and the wetting phase film,

$$L_{nw1} = 2r_d \sum_{i=1}^n \left(\frac{\pi}{2} - \frac{\varepsilon_i}{2} - \theta^*\right)\delta_i, \tag{20}$$

$$L_{nw2} = (P - 2r_d S_1) f_{ly}(1 - f_{lx}) + (P - 2r_d S_1)(1 - f_{ly}) f_{lx}, \tag{21}$$

$$L_{nw} = L_{nw1} + L_{nw2} = 2r_d S_2 + u(P - 2r_d S_1), \tag{22}$$

where $S_2 = \sum_{i=1}^n \left(\frac{\pi}{2} - \frac{\varepsilon_i}{2} - \theta^*\right)\delta$, and $u = 1 - f_{lx}f_{ly}$. The length of dashed line is approximately equal to the red line of border region in Fig. 6(b) in calculating the film length of the smooth capillary cross-section.

Next, we calculate the non-wetting phase area in the inner and border regions, respectively:

$$A_{nw1} = A - r_d^2(\cos\theta^* S_1 - S_2), \tag{23}$$

$$A_{nw2} = L_{nw2}(h - h_w) = u(P - 2r_d S_1)(h - h_w), \tag{24}$$

$$A_{nw} = A_{nw1} + A_{nw2} = A - r_d^2(\cos\theta^* S_1 - S_2) + w(P - 2r_d S_1). \tag{25}$$

where $w = u(h - h_w)$. From Eq. (4), the MS-P method finally gives,

$$\frac{2r_d S_2 + u(P - 2r_d S_1) + v(P - 2r_d S_1)\cos\theta}{[A - r_d^2(\cos\theta^* S_1 - S_2) + w(P - 2r_d S_1)]} = \frac{1}{r_d} \tag{26}$$

And we can simplify it to the form of Eq. (11):

$$[(2u + 2v\cos\theta - \cos\theta^*)S_1 - S_2]r_d^2 - [(u + v\cos\theta)P + 2wS_1]r_d + (wP + A) = 0 \tag{27}$$

When the surface is smooth, $r_f = 1, f_{lx} = 1, f_{ly} = 1, h_w = h$, then $\theta = \theta^*$, $u = 0$, $w = 0$, and $v = 1$. It follows that Eq. (27) reduces to,

$$[(2u + 2v\cos\theta - \cos\theta^*)S_1 - S_2] = \cos\theta S_1 - S_2 = f_T, \tag{28}$$

$$[(u + v\cos\theta)P + 2wS_1] = P\cos\theta, \quad (wP + A) = A. \tag{29}$$

Comparing Eq. (27) with Eq. (11) in such case, we find they are equivalent, which means that, for smooth capillaries, Eq. (11) can be recovered from Eq. (27). By solving Eq. (27), we can obtain the threshold drainage radius and calculate the capillary entry pressure by
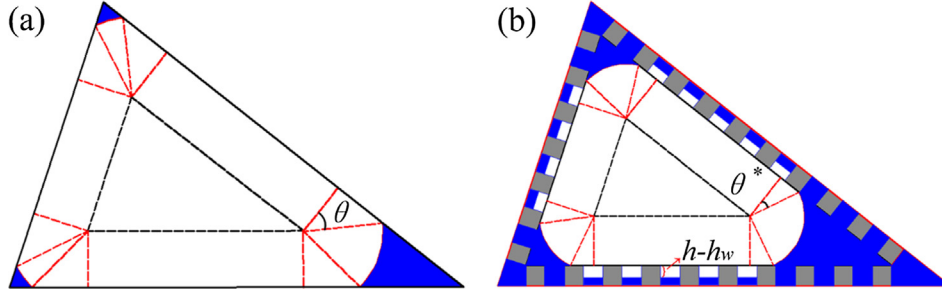
Fig. 5. Phase distribution in different cross-sections during drainage, the blue block means the wetting phase and the white means the non-wetting phase (a) cross-section in a smooth capillary (b) cross-section in a rough capillary, θ^*. is the apparent contact angle. (For interpretation of the references to color in this figure legend, the reader is referred to the web version of this article.)

Eq. (5). Moreover, the saturation can be calculated by:

$$S_w = 1 - A_{nw}/[(A_0(1-f_{ly}) + f_{ly}(A_0-f_{lx}P_0h)].$$ (30)

4. Model verification

To solve Eq. (27), we first have to identify two parameters: i.e., the apparent contact angle and the wetting phase film height. In this section, we obtain these two parameters by the Lattice Boltzmann method (LBM) simulation. Moreover, the capillary entry pressure in rough capillaries are analyzed using LBM simulation and then we compare the semi-analytical model against numerical simulation results.

4.1. Shan-Chen multicomponent Lattice Boltzmann model

The Lattice Boltzmann method is a pseudo-molecular method that tracks the evolution of the particle distribution function of an assembly of molecules. For single-phase flow, it follows the LBGK evolution equation derived from the Boltzmann equation (Bhatnagar et al., 1954),

$$f_i(\mathbf{x} + \mathbf{e}_i\Delta t, t + \Delta t) = f_i(\mathbf{x},t) - \frac{1}{\tau}(f_i(\mathbf{x},t) - f_i^{eq}(\mathbf{x},t)),$$ (31)

where $f_i^{eq}(\mathbf{x},t)$ is the density distribution function, $\mathbf{x}$ is the spatial position, $\mathbf{e}_i$ is the discrete velocity along the ith lattice direction, τ is the relaxation time, and $f_i^{eq}(\mathbf{x},t)$ is the corresponding equilibrium distribution function.

The equilibrium distribution functions depend on the particular velocity model and can be calculated as

$$f_i^{eq}(\mathbf{x},t) = \omega_i\rho\left[1 + \frac{\mathbf{e}_i\cdot\mathbf{u}}{c_s^2} + \frac{(\mathbf{e}_i\cdot\mathbf{u})^2}{2c_s^4} - \frac{\mathbf{u}^2}{2c_s^2}\right],$$ (32)

where w_i s are weights and c_s is the sound speed. ρ and $\mathbf{u}$ are the macroscopic density and the macroscopic velocity vector respectively, which can be calculated from:

$$\rho = \sum_i f_i, \quad \mathbf{u} = \frac{1}{\rho}\sum_i f_i\mathbf{e}_i.$$ (33)

The Shan-Chen multiphase Lattice Boltzmann model (or the pseudopotential multiphase model) was originally proposed by Shan and Chen (Shan and Chen, 1993; Shan and Chen, 1994), and its intermolecular interactions are represented by a density-dependent pseudopotential. It includes two kinds of models, namely single-component multiphase (SCMP) model and multicomponent multiphase model (MCMP) (Sukop and Thorne, 2006). As the MCMP model is used in later verifications, here we only introduce the MCMP model for the sake of conciseness.

In the MCMP Lattice Boltzmann model, each fluid component follows a similar LBGK evolution equation (Eq. (31)) as in single-phase flow. The equilibrium velocity of the σ th component is modified to carry the effect of the interactive and adhesive forces:

$$\mathbf{u}^{eq} = \mathbf{u}' + \frac{\tau_\sigma(F_{\text{int},\sigma} + F_{\text{ads},\sigma})}{\rho_\sigma},$$ (34)

where $F_{\text{int},\sigma}$ is the fluid-fluid interactive force between different components, $F_{\text{ads},\sigma}$ is the fluid-solid interactive force, and $\mathbf{u}'$ is a composite macroscopic velocity defined as $\mathbf{u}' = \sum_\sigma (\sum_i \frac{f_i^\sigma \mathbf{e}_i}{\tau_\sigma})/(\sum_i \frac{\rho_i^\sigma}{\tau_\sigma})$.

In order to simulate separation between different components in multicomponent fluids, non-local interactions between fluid particles are incorporated via the following fluid-fluid interactive force,

$$\mathbf{F}_{\text{int},\sigma}(\mathbf{x},t) = -\rho_\sigma(\mathbf{x},t)G_{\text{int},\sigma\bar{\sigma}}\sum_i \omega_i\rho_{\bar{\sigma}}(\mathbf{x} + \mathbf{e}_i\Delta t,t)\mathbf{e}_i,$$

where σ and $\bar{\sigma}$ represent different components and $G_{\text{int},\sigma\bar{\sigma}}$ is a parameter that controls the interaction force between the different components.

The adhesive or solid surface force on the σ th component can be computed as follows (Martys and Chen, 1996):

$$\mathbf{F}_{\text{ads},\sigma}(\mathbf{x},t) = -G_{\text{ads},\sigma}\rho_\sigma(\mathbf{x},t)\sum_i \omega_i s(\mathbf{x} + \mathbf{e}_i\Delta t,t)\mathbf{e}_i,$$ (35)

where the $s(\mathbf{x} + \mathbf{e}_i\Delta t,t)$ is an indicator function that is equal to 1 or 0 for a solid or fluid domain node, $G_{\text{ads},\sigma}$ is a parameter that controls the strength of the interfacial tension between the solid and σ th component.
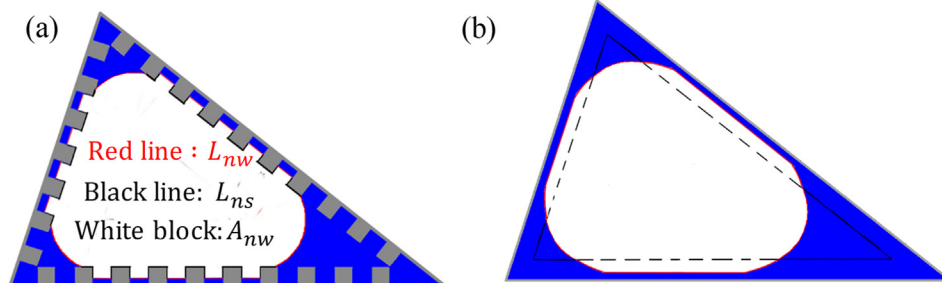

Fig. 6. Fluid configurations in a rough capillary, (a) rough capillary cross-section; such a cross-section appears along the y-axis direction with a probability of f_{ly} (b) smooth capillary cross-section; such a cross-section appears in a probability of 1-f_{ly}.

4.2. Wetting theory on rough surfaces: Logistic model

The well-known Wenzel model and Cassie-Baxter model have been reported to only be applicable to certain conditions (Morrow, 1975; Milne and Amirfazli, 2012; Carmeliet et al., 2017). For example, the drop size must be sufficiently large compared with the surface roughness scale for the Wenzel equation and the Cassie–Baxter equation is only correct for the case of flat topped pillar geometry without any penetration of the liquid. Based on previous understanding of physical mechanisms on rough surface wetting theory, we propose a new equation for Wenzel state from the perspective of mathematical modeling.

As the Young's contact angle is always smaller than 90° when non-wetting phase invades the wetting phase in the described semi-analytical model, we only need to model the wetting behavior of hydrophilic rough surfaces, on which the droplet always stay in Wenzel state (Bico et al., 2002). Logistic population growth is a famous model to predict population. In the Logistic model, the carrying capacity restricts the population from growing infinitely, and population regulation is a density-dependent process, meaning that population growth rates are regulated by the density of a population (Verhulst, 1845). Denote the maximum value of Young's contact angle θ that makes the apparent contact angle decrease to 0 as θ_c on a rough surface, i.e., when Young's contact angle is smaller than this critical value, the apparent contact angle is always 0. When $\theta > \theta_c$, assuming θ^* increases with roughness factor r_f on a rough surface, and the growth rates are related to θ and the "carrying capacity" $\theta^*_{max} = 90°$, then the Logistic model is,

$$\theta^* = \frac{90}{1 + \frac{90-\theta}{\theta-\theta_c}e^{m(r_f-1)}}, \theta > \theta_c \tag{36}$$

where m is the growth rate, θ_c is the critical contact angle, and they both depend on the design of the rough surface.

We design three rough surfaces according to Fig. 3, namely $h = 1$, $a = b = d = 2$; $h = 2$, $a = b = d = 2$ and $h = 4$, $a = b = d = 2$. The roughness factors are 1.5, 2, and 3, respectively. The Shan-Chen multicomponent Lattice Boltzmann model is initialized to mimic wetting behaviors on both smooth and rough surfaces. The D3Q19 velocity model is used and the major density for wetting phase or non-wetting phase is 8.0, $G_{int,\sigma\bar{\sigma}} = 0.225$ and different wetting conditions are achieved by adjusting $G_{ads,\sigma}$. The simulation domain size is $120 \times 120 \times 80$ and the initial droplet size is 30. Bounce-back boundaries are applied to the solid walls and the other boundaries are periodic. Three simulation results when $r_f = 3$ are shown in Figs. 7 and 8 summarizes data concerning all the results for the three rough surfaces. We also do curve fitting between Young's contact angles and the apparent contact angle based on Eq. (36); the curves match well with simulation results. Further, the growth rate and critical contact angle on this type of rough surface are given by:

$$m = (0.55\ln r_f + 0.016)/(r_f-1), \quad \theta_c = 30.5\ln r_f. \tag{37}$$

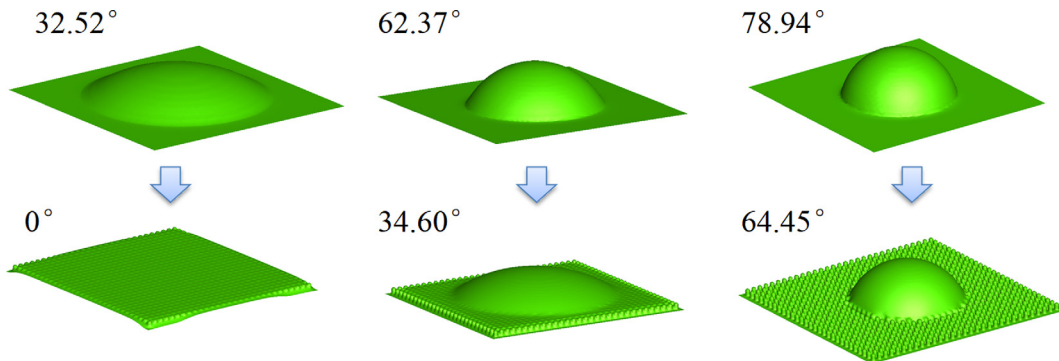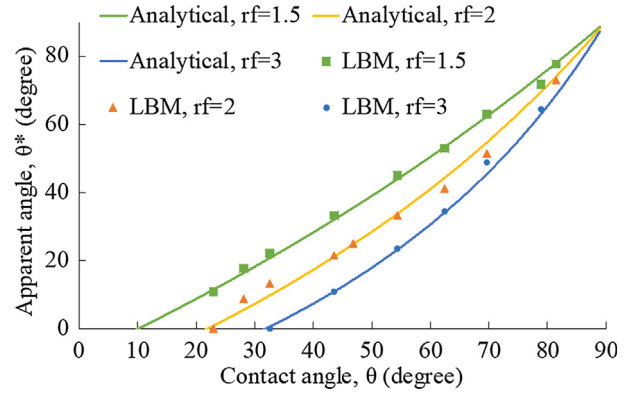**Fig. 8.** Relation between Young's contact angles on a smooth surface and the corresponding apparent contact angles on a rough surface.
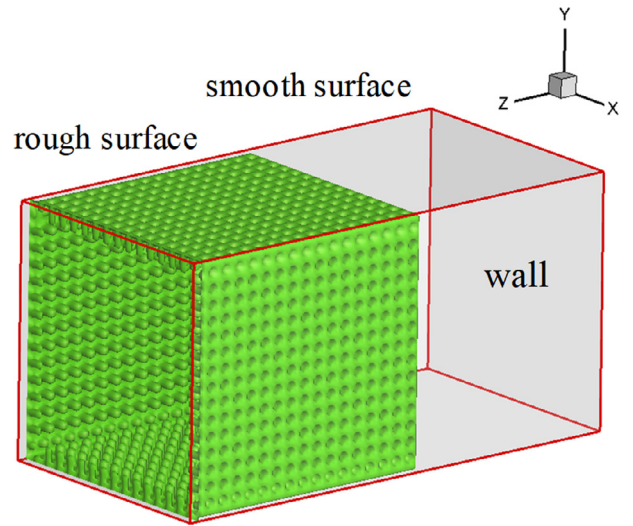

Fig. 9. A half-rough and half-smooth tube used to mimic a capillary-rise like process. The cross section can be arbitrary and square is just an example.

4.3. Fluid distribution in rough capillaries under quasi-static

In this section, we observe the steady fluid distribution in rough capillaries using the Shan-Chen LB model. A half-rough and half-smooth tube with a solid bottom is designed, as shown in Fig. 9. In simulation, the smooth half is initialized with wetting phase and the rough half with non-wetting phase. The redistribution of fluid is then calculated by LBM, similar to a capillary-rise process. Fig. 10 compares two different fluid configurations from simulations. In Fig. 10(a), the AMs appear in corners while this would never happen for the smooth
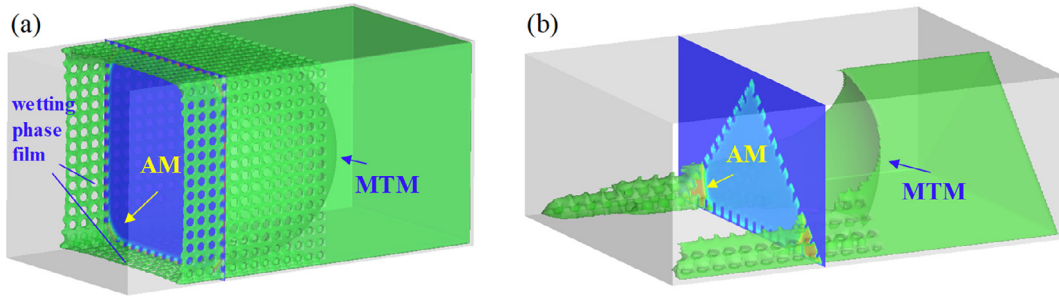

Fig. 7. Young's contact angles on smooth surfaces and the corresponding apparent contact angles on rough surfaces with $r_f = 3$.

Fig. 10. Fluid configurations simulated by Shan-Chen LB model in rough capillaries, (a) square cross section with $\theta = 45°$ and $r_f = 3$. Except the AMs in the corner, there are also wetting phase films on the wall surfaces. (b) cross-section of isosceles right triangle with $\theta = 62°$ and $r_f = 1.6$. There almost no wetting phase films on walls and AMs only appear in the 45° base angles.

capillary when $\theta = 45°$ (see Eq. (9)). This is because the rough surface decreases the contact angle so that AMs can form with an apparent contact angle smaller than 45°. It is also notable that there are wetting phase films around the wall surfaces, which is consistent with the assumption in Section 3. In Fig. 10(b), we give an example of the fluid distribution in a pore of isosceles right triangular cross-section where the upper angle is 90°; the roughness factor is smaller and the apparent contact angle is not small enough to form AM in the right angle, but it is wetting enough to form AMs in the 45° base angles. Meanwhile, there almost no wetting phase films on the walls for the poor wetting condition.

We can also measure the wetting phase film height by calculate the density in grooves of the tube slice. As the density profile in the tube is continuous in the LBM simulation results, the film height can be estimated by the quotient of the wetting phase density in one groove divided by the major density of the wetting phase (around 8.0) in the equilibrium state. Fig. 11 gives an example of wetting phase density profile of tube slices when $h = 4$. Similar with the results in Fig. 10, there are almost no wetting film in grooves when $\theta = 62.37°$, while the films exist when $\theta = 45°$. We also fit a curve between Young's contact angle and film height based on LBM simulation, which demonstrates that it is a sigmoid-like curve as shown in Fig. 12. The wetting film height as a function of Young's contact angle satisfies

$$h_w = \left(1 - \frac{1}{1 + e^{-0.12(\theta-45)}}\right)h. \tag{38}$$

Note that in a vapor-fluid system in capillaries, there are also film adsorption on surfaces (either in smooth surface or rough surface), but mainly determined by disjoining pressure. We cannot consider this feature in this model and Tuller et al. (1999) gave more details on the adsorption and capillary condensation in porous media.

4.4. Capillary entry pressure in rough capillaries

As oblique lines in the regular lattice grid system leads to zigzag boundaries during LB simulation, we use square capillary rather than triangular capillary to verify the semi-analytical model in this section. A whole-smooth or whole-rough capillary tube with domain size of $64 \times 64 \times 120$ (note that the inscribed circle radius of cross section is 31 because the edge is solid) is designed as shown in Fig. 13. The capillary is full of wetting phase at the simulation beginning with density
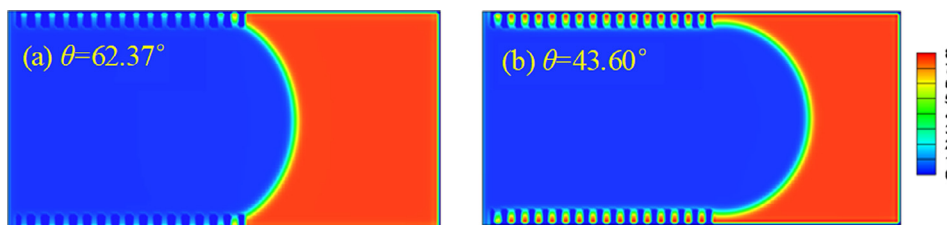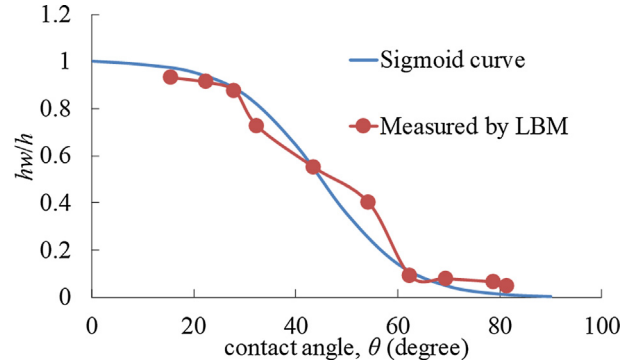

Fig. 12. Wetting film height as a function of Young's contact angle, LBM simulations and curve fitting.

of 8.0, and we meanwhile add non-wetting/wetting phase reservoirs on the top/bottom consisting of additional three layers. By droplet test, the interface tension γ_{nw} was calculated by Laplace's law and the value is 0.9458 when the major density is 8.0 for each phase. Pressure boundary conditions (equivalent to densities) are applied to the first layer of the non-wetting phase reservoir and the last layer of the wetting phase reservoir. To simulate the primary drainage process, we started from zero capillary pressure, which was achieved by fixing non-wetting phase and wetting phase densities in the first layer and last layer of the reservoir, respectively (Pan et al., 2004, Zhang et al., 2016). The density on the bottom was fixed at 7.95 and the density on the top was increased from 7.95 to 8.40. The driving pressure increased gradually and non-wetting phase began to enter the tube and displace the wetting phase in the initially wetting-phase-saturated capillary.

Finally, we obtain a series of P_c/γ_{nw}-S_w curves for the smooth and rough capillaries, under different wetting conditions and with different roughness factors. Then we can compare the simulated and analytical entry pressure, and here we take the rough one when $r_f = 3$ ($h = 4$, $a = b = d = 2$) as an example. When $\theta = 32.52°$, $h_w = 0.725\,h$ and apparent angle $\theta^* = 0$, the analytical entry pressure P_c/γ_{nw} calculated from extended MS-P model from Section 3 for a rough capillary is 0.0695 and that for a smooth capillary calculated from general MS-P method is 0.0536. Primary drainage curves obtained by LBM simulations under the same conditions are shown in Fig. 14, in which we can
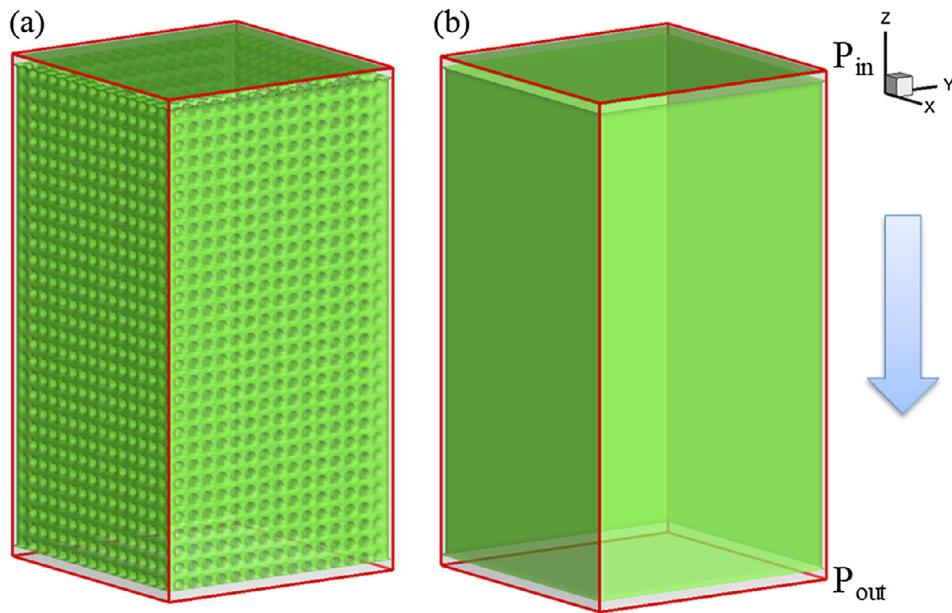

Fig. 11. Density profile of wetting phase in tube slices for different wetting conditions.

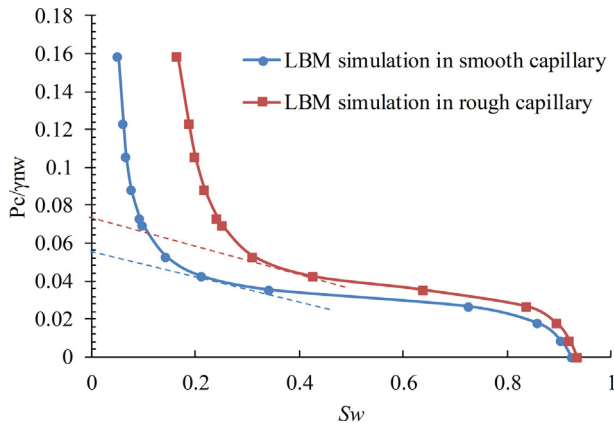**Fig. 13.** Rough and smooth capillaries with square cross section designed for verifying the analytical model.

Fig. 14. Primary drainage curves obtained by fluid displacement simulations when $\theta = 32.52°$, the rough capillary was designed with a rough surface when $r_f = 3$. The curve can be divided into three stages, i.e., the two steeply increasing stages at the initial and end of the drainage and the middle steady growth stage. The dashed tangent lines are made at the end of middle steady growth stage.

Fig. 15. Comparison of entry pressure between LBM simulations and analytical models.

make a tangent line at the inflection point (not the point where the second derivative is equal to 0 but the point where the curve become much steeper) of the capillary pressure curve; the intersection point between the tangent line and y-axis is the capillary entry pressure, the value is 0.0720 and 0.0560, for the rough capillary and the smooth one, respectively. The relative error is smaller than 5% and we obtain good agreement of the simulated and analytical entry pressure.

Fig. 15 summarizes another five pairs of simulation results against the semi-analytical model, though the relative error is larger than 5% in some cases, there is good agreement overall. We also give three displacement processes driven by the entry pressure in a rough capillary under different wetting conditions (corresponding to the cases in Fig. 7) to show the differences. It can be seen from Fig. 16 that the non-wetting phase enters the middle channel for low flow resistance, then the non-wetting phase tries to penetrate into the grooves on the rough surface. However, due to the wetting film adsorbed on the walls, the non-wetting phase can only penetrate partly under strong wetting conditions (Fig. 16(a)). While in the case when the wetting condition is not strong enough, the non-wetting phase can fill most grooves on the surface, and
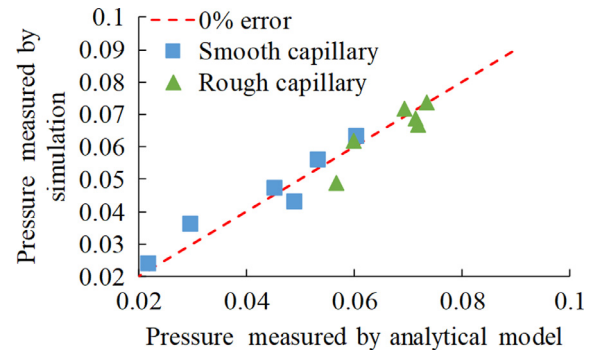
the displacement process like a two-step layered flow: fill the middle first and then the surface (Fig. 16(b)). Moreover, when the wettability becomes poorer, the non-wetting phase even can penetrate the grooves at the first step (Fig. 16(c)).

4.5. Contact angle hysteresis in rough capillaries

The contact angle hysteresis is influenced by many mixing factors, such as the droplet size, flow velocity, as well as the surface roughness and it's hard to illustrate it separately. In this section, we will only discuss the contact angle hysteresis in few rough capillaries under small pressure difference.

There are usually three ways in literatures to study the contact angle hysteresis (usually measured by the difference between the advancing contact angle and receding contact angle):

(1) Slowly increasing the volume of a drop or sucking the liquid and observing contact lines (Gao and McCarthy, 2006). During the increase of drop volume, the contact line first remains stuck before it suddenly jumps above a critical volume. The maximum observed angle is the so-called advancing contact angle θ_A. If we afterwards decrease the volume of the drop and determine the contact angle just before the wetting line is receding, we measure the so called receding contact angle, θ_R.

(2) Droplet moving driven by the body force or external force. The
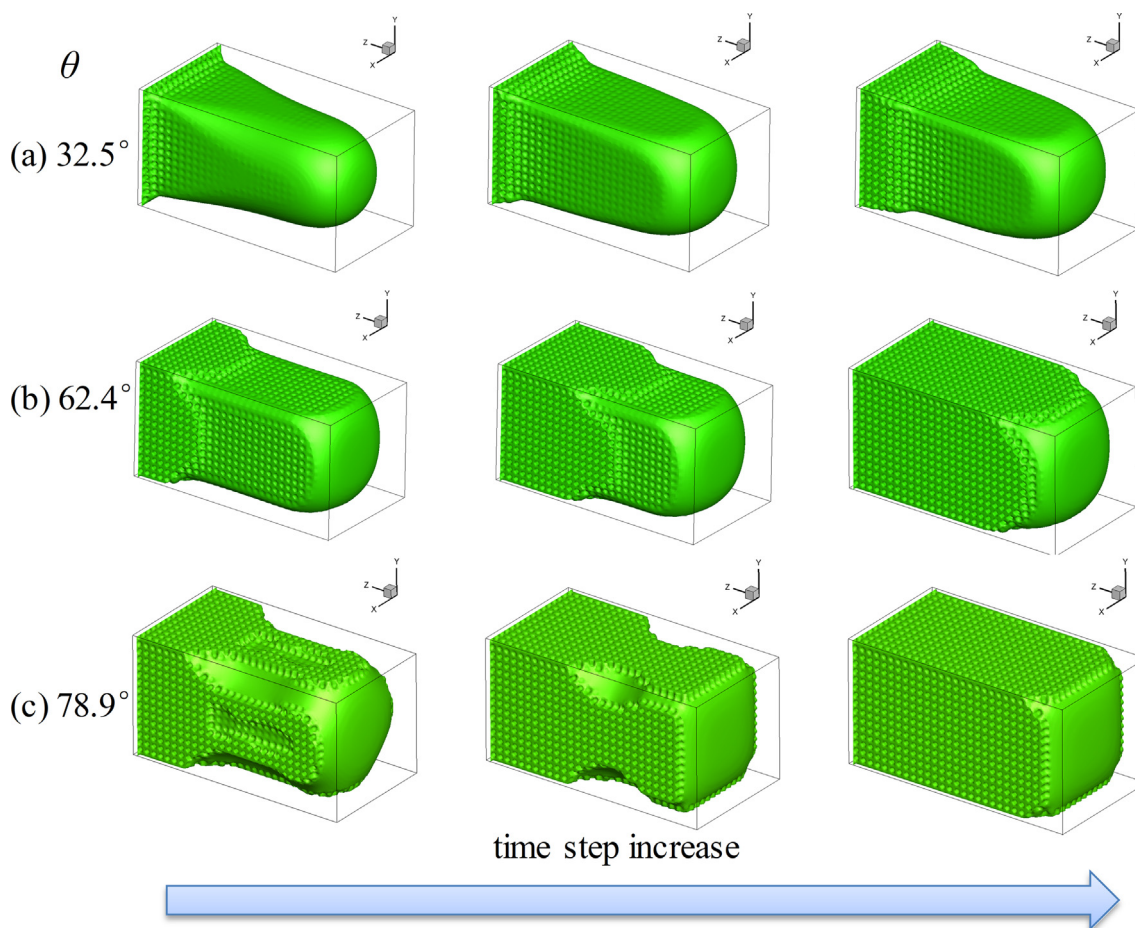
Fig. 16. Displacement process driven by the entry pressure in a rough capillary under different wetting conditions. The green color represents the non-wetting phase. (For interpretation of the references to color in this figure legend, the reader is referred to the web version of this article.)

contact angle is different at the front and at the rear of the drop. Contact line always stays stationary and the droplet only deforms if the instantaneous receding contact angle and advancing contact angle don't arrive certain critical values. Ba et al. (2016) studied the contact angle hysteresis on topologically structured surfaces using LBM and analyzed the critical capillary number for droplet slipping.

(3) Liquid column motion due to capillary force, such as measuring the contact angles by Wilhelmy plate method. The measure of receding contact angle or advancing contact angle depends on the relative movement direction of the plate.

In our study, we focus on the contact hysteresis in a capillary, so we construct a similar model according to Joanny and De Gennes (1984), i.e., a wetting phase column is initialized in the middle of a capillary, while the other space is filled with non-wetting phase. Pressure boundary conditions are applied to inlet and outlet and the pressure difference is relatively small than the capillary entry pressure (eliminate the effects of large flow velocity.), so that the non-wetting phase will invade the wetting phase from both capillary ends, forming the advance receding contact angle and advancing contact angle, as shown in Fig. 17(a). In the following simulation, we only consider the similar capillaries in Section 4.4, the domain size of the capillary is $64 \times 64 \times 128$, the inlet and outlet are non-wetting reservoir consisting of 20 layers, the 21th layers-108th layers along the z axis is the capillary. Before simulation, the 40th–90th layers are filled with wetting phase, and the first layer density of inlet and outlet are fixed at 8.03 and 8.0, respectively, as shown in Fig. 17(b).

Contact angle hysteresis under different wetting conditions ($\theta = 78.9°$, 62.3°, and 32.5°) in different rough capillaries ($r_f = 1, 1.5,$

2, and 3) are simulated by LBM, the results are shown in Fig. 18. Firstly, it can be seen that the roughness decreasing the advancing and receding contact angle simultaneously. Then by measuring receding contact angle in rough capillaries, we find that the receding contact angle is close to the corresponding apparent contact angle in strong wetting conditions. While the receding contact angle in poor wetting conditions seems tend to larger than the corresponding apparent angle, which maybe is due to the limited simulation time step. In addition, the difference between the advancing contact angle and receding contact angle (contact hysteresis) stays relative stable and do not show a clear changing pattern. In brief, in our simulations, we can say that the roughness can decreasing the receding contact angle further, but it does not mean the roughness is bound to promote the contact hysteresis. Moreover, if the contact angle hysteresis is ignored in the new proposed model, the accuracy may be influenced in poor wetting conditions.

5. Results and discussion

Define the dimensionless capillary entry pressure as:

$$P_{cnorm} = P_{cr}/P_{cs},$$

where P_{cs} is the capillary entry pressure in a smooth capillary and P_{cr} is the capillary entry pressure in a rough capillary of the same size (refer to capillaries in Fig. 5).

Introduce five dimensionless variables to describe how the roughness influences the capillary entry pressure in different wetting conditions:

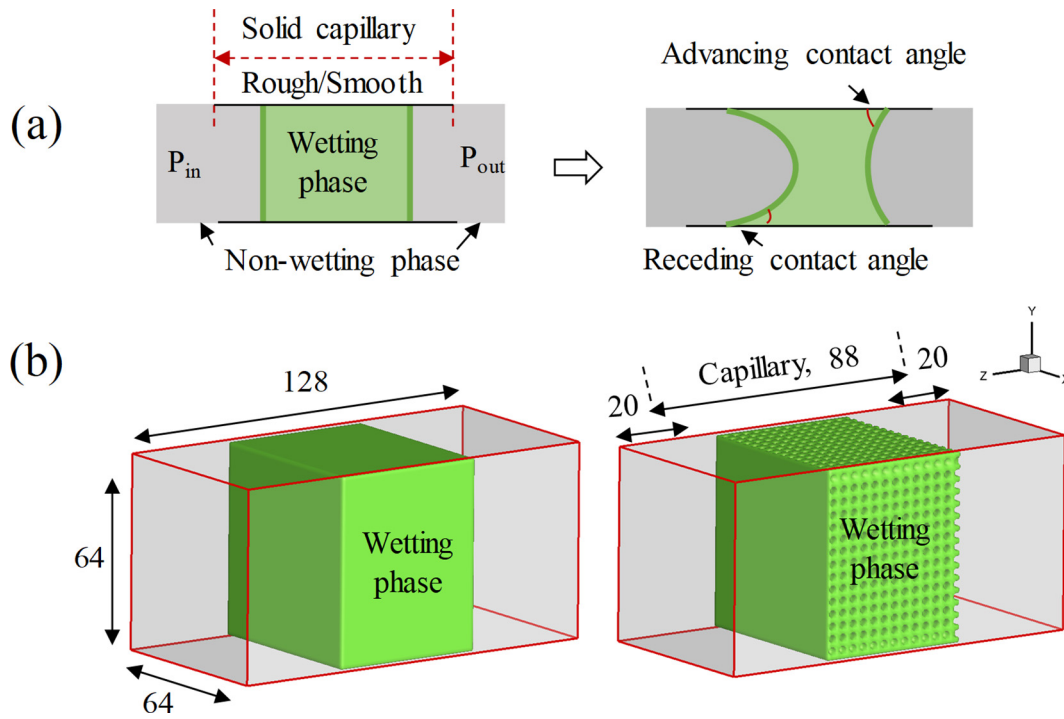$$\alpha = a/d, \beta = b/d, \omega = d/P_0, \lambda = h/r_{in}, G = A_0/P_0^2,$$

Fig. 17. Simulation initialization of contact angle hysteresis in a capillary.
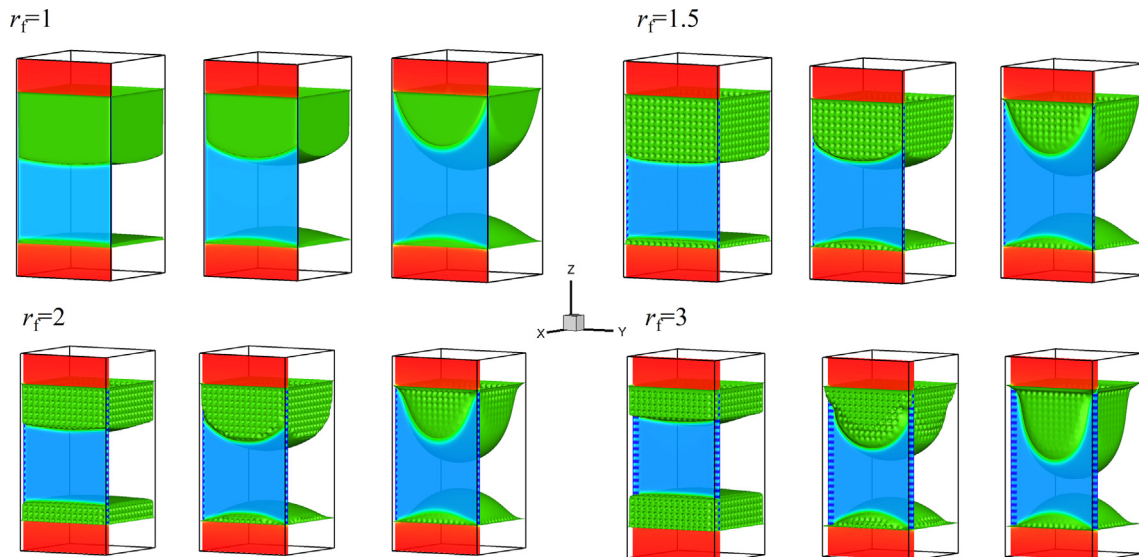

Fig. 18. Contact angle hysteresis in capillaries with different roughness factor (simulation time step at 50000). Each case is modified with three different wetting conditions, the Young's contact angle from left to right is 78.9°, 62.3°, and 32.5° respectively. The green block represents non-wetting phase and the slices closest to the solid walls are shown. (For interpretation of the references to color in this figure legend, the reader is referred to the web version of this article.)

where r_{in} is the inscribed radius of the polygon and G is the shape factor.

We take triangles as examples to analyze the influencing factors in this section. The triangles can be constructed using method Patzek's (2001). For convenience, the inscribed radius of the triangle is set to one. Also, readers can refer to Wei's (2015) method if n-sided polygon construction is needed (Wei et al., 2015). The apparent angles and film height are calculated by Eqs. (36)(38).

5.1. Analysis of influencing factors: groove length and groove width

Let $h = 0.1$, $b = 0.05$ (or $a = 0.05$), $d = 0.05$, $G = 0.024$, then construct various shapes with different groove length (or groove width), leading to various values of α (or β). After this, calculate capillary behaviors using the proposed model in Section 3. α and β can indicate the impact of groove length and groove width on the capillary behavior respectively. Fig. 19 gives the information concerning how P_{cnorm} changes with groove length and contact angle. Overall, P_{cnorm} is larger than one, which means that the rough capillary entry pressure is always larger than the smooth one under the same conditions. Moreover, P_{cnorm} shows a dramatic rise with the increase of contact angle; however it remains stable at different values of α when the contact angle is smaller than 40°. This is because the reciprocal of $\cos\theta$ is greater when the contact angle is bigger. Meanwhile the rough surface would make the contact angle smaller and the range of the drop is much bigger under poor wetting conditions than that in good wetting conditions; that is to say, $\cos\theta^*/\cos\theta$ plays a key role in this rising trend and
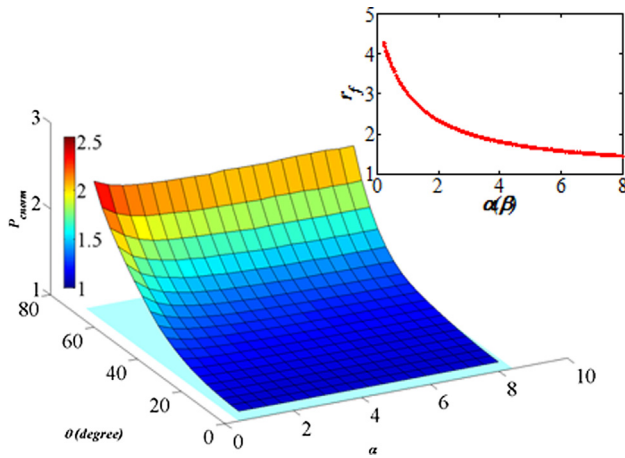
Fig. 19. Influence of asperity length on the dimensionless capillary entry pressure under different wetting conditions.

Fig. 21. Influence of asperity height on the dimensionless capillary entry pressure under different wetting conditions.

the rough surface can't decrease the apparent angle significantly. P_{cnorm} also decreases a little with the increase of α for the gradually declining roughness factor. However, it is clear from the subgraph of Fig. 19 that there is a dramatic decline in r_f with the increase of α, which means that α has little influence on P_{cnorm}, even under poor wetting conditions. Though there is a subtle difference due to the drainage direction (i.e., the influence of f_{ly}), our results indicate that the influence of groove width on the capillary behavior is similar to that of groove length, for they exert the similar impact on r_f according to the subgraph in Fig. 19.

5.2. Analysis of influencing factors: Asperity width

Similarly, let $a = 0.05$, $b = 0.05$, $h = 0.1$, $G = 0.024$, then construct various shapes with different asperity width, leading to various values of ω. Thus ω illustrates the influence of asperity width. Fig. 20 summarizes the simulation results in terms of how P_{cnorm} changes with ω under different wetting conditions. P_{cnorm} grows noticeably with the rise of contact angle at small ω while it declines with ω when the contact angle is large enough. It increases gradually at its initial stage and then peaks at a certain point with the increase of ω. After the peak point, it decreases gradually. This is because the roughness factor fluctuates with ω in a similar pattern, as shown in the subgraph of Fig. 20. In addition, the degree of decrease is larger than the influence of α in Section 4.1. P_{cnorm} is still not sensitive to the roughness factor under strong wetting conditions.
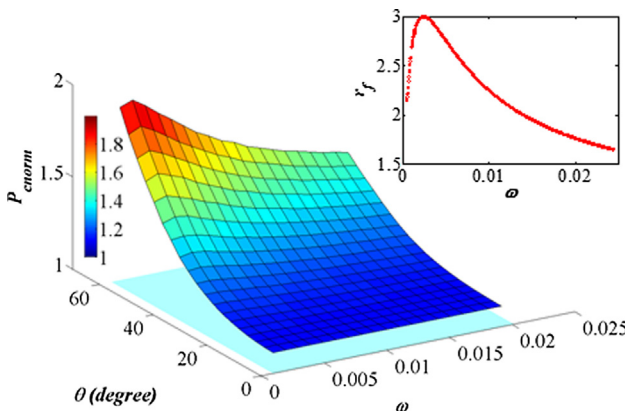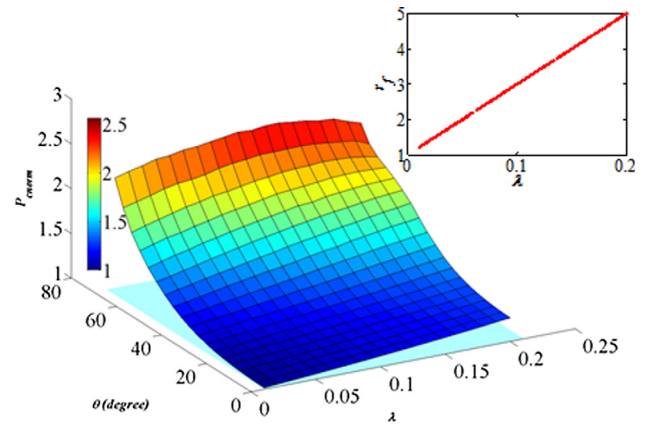
5.3. Analysis of influencing factors: Asperity height

Construct various shapes with different asperity height, making sure that $a = 0.05$, $b = 0.05$, $d = 0.05$ and $G = 0.024$. Fig. 21 compares the statistics regarding the capillary behaviors in rough capillaries when the asperity height and contact angle vary. Then λ can illustrate the influence of asperity height. In general, P_{cnorm} increases with λ and contact angle. However, there is a slight drop for P_{cnorm} with the increase of λ under poor wetting conditions. This can happen when the roughness factor is large enough and decreases the apparent angle significantly under poor wetting conditions. Moreover, it seems that λ exerts more impacts on this upward trend than α and ω, for it decreases the effective radius of capillary directly.

5.4. Analysis of influencing factors: Shape factor

Shape factor has an important influence on the wetting phase saturation. Construct different shapes making sure that $a = 0.05$, $b = 0.05$, $d = 0.05$ and $h = 0.1$. Fig. 22 provides statistics concerning the performance of the wetting saturation of these shapes in rough and smooth capillaries. As shown in Fig. 22, the wetting saturation in rough capillaries is larger than in smooth capillaries. Two combined factors contribute to this: on the one hand, the rough surface narrows the pore space, and the grooves are filled with wetting phase film; on the other hand, the rough surface would make the apparent contact angle smaller, which means more wetting phase could exist in the corners. In addition, the wetting saturation in rough capillaries shows a similar trend with that in smooth capillaries, i.e., the wetting saturation decreases with the shape factor and the contact angle. This is because the bigger the shape factor is, the more regular the shape is, and as a result,
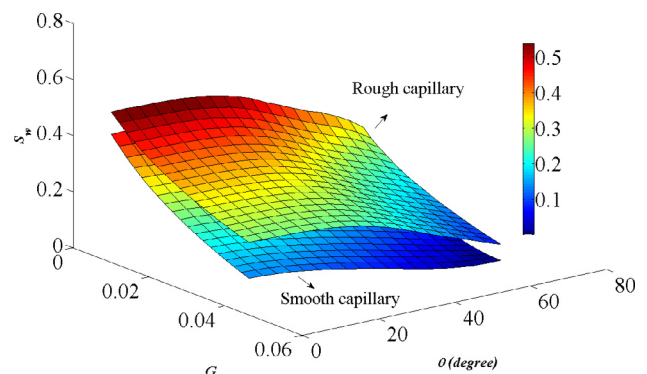

Fig. 20. Influence of groove width on the dimensionless capillary entry pressure under different wetting conditions.

Fig. 22. Influence of shape factor on the wetting saturation under different wetting conditions.

there would be less corner space to hold wetting phase. Also, the increasing contact angle would narrow the space of wetting phase in the corners, which is stated clearly by Wei et al. (2015). There is a slight difference in that the wetting phase in rough capillaries would decrease more quickly after a certain point with the increase of the contact angle.

To conclude, both the wetting phase saturation and entry pressure of rough capillaries are always larger than those of smooth ones under the same conditions, and Fig. 14 show good evidence of this point. Furthermore, the capillary entry pressure is not sensitive to the roughness factor under strong wetting conditions. As to the magnitude of their relative effects on rough capillary entry pressure under middle or poor wetting conditions, the contact angle ranks first, then the asperity height, followed by the asperity width, and groove length/width is last.

6. Conclusions

To sum up, we propose a semi-analytical model based on the MS-P and wetting theories of rough surfaces to calculate the capillary entry pressure in rough capillaries with polygonal cross-sections. We provide a new Logistic wetting equation to calculate the apparent contact angle in the Wenzel state and to verify the model with Lattice Boltzmann method simulations. Using this model, we discuss capillary behavior under different conditions.

First, both the wetting phase saturation and entry pressure of rough capillaries are larger than those of smooth ones under the same conditions. The effective radius of the capillary would decrease and the contact angle would be smaller in the rough capillary. Meanwhile the rough surface would also change the phase distribution, for example, there would be a wetting phase film adsorbed on surface.

Moreover, the contact angle and asperity height have a more significant influence on capillary entry pressure than any other factors, followed by asperity width and groove length/width. In general, the capillary entry pressure changes only slightly with the roughness factor under strong wetting conditions.

Acknowledgments

References

Afferrante, L., Carbone, G., 2014. The effect of drop volume and micropillar shape on the apparent contact angle of ordered microstructured surfaces. Soft Matter. 10, 3906–3914.

Al-Anssari, S., Barifcani, A., Wang, S., Maxim, L., Iglauer, S., 2016. Wettability alteration of oil-wet carbonate by silica nanofluid. J. Colloid Interface Sci. 461, 435–442.

Badge, I., Bhawalkar, S.P., Jia, L., Dhinojwala, A., 2013. Tuning surface wettability using single layered and hierarchically ordered arrays of spherical colloidal particles. Soft Matter 9, 3032–3040.

Ba, Y., Kang, Q., Liu, H., Sun, J., Wang, C., 2016. Three-dimensional Lattice Boltzmann simulations of microdroplets including contact angle hysteresis on topologically structured surfaces. J. Comput. Sci. 17, 418–430.

Bhatnagar, P.L., Gross, E.P., Krook, M., 1954. A model for collision processes in gases. I. Small amplitude processes in charged and neutral one-component systems. Phys. Rev. 94 (3), 511.

Bico, J., Thiele, U., Quéré, D., 2002. Wetting of textured surfaces. Colloids Surf. A 206 (1), 41–46.

Blunt, M.J., Jackson, M.D., Piri, M., Valvatne, P.H., 2002. Detailed physics, predictive capabilities and macroscopic consequences for pore-network models of multiphase flow. Adv. Water Resour. 25, 1069–1089.

Bormashenko, E., 2015. Progress in understanding wetting transitions on rough surfaces. Adv. Colloid Interface Sci. 222, 92–103.

Butt, H.J., 2008. Capillary forces: influence of roughness and heterogeneity. Langmuir 24, 4715–4721.

Carmeliet, J., Chen, L., Kang, Q., Derome, D., 2017. Beyond-cassie mode of wetting and local contact angles of droplets on checkboard-patterned surfaces. Langmuir 33 (24), 6192.

Cassie, A.B.D., 1948. Contact angles. Discuss. Faraday Soc. 3, 11–16.

Chandra, D., Yang, S., 2011. Dynamics of a droplet imbibing on a rough surface. Langmuir 27, 13401–13405.

Chowdhury, I., Hong, Y., Honda, R.J., Walker, S.L., 2011. Mechanisms of TiO2 nanoparticle transport in porous media: role of solution chemistry, nanoparticle concentration, and flowrate. J. Colloid Interface Sci. 360, 548–555.

Extrand, C.W., 2007. Retention forces of a liquid slug in a rough capillary tube with symmetric or asymmetric features. Langmuir 23, 1867–1871.

Gao, L., McCarthy, T.J., 2006. Contact angle hysteresis explained. Langmuir 22 (14), 6234–6237.

Guo, Q., Liu, Y., Jiang, G., Zhang, X., 2014. Condensation of droplets on nanopillared hydrophobic substrates. Soft Matter 10, 1182–1188.

Hanspal, N.S., Allison, B.A., Deka, L., Das, D.B., 2013. Artificial neural network (ANN) modeling of dynamic effects on two-phase flow in homogenous porous media. J. Hydroinform 15, 540–554.

Hecht, K., Messerschmidt, F., Pfeifer, P., Dittmeyer, R., Kraushaar-Czarnetzki, B., Hecht, S., 2013. Surface roughness of machined microchannels and its effect on multiphase boundary conditions. Chem. Eng. J. 227, 2–12.

Hoła, J., Sadowski, Ł., Reiner, J., Stach, S., 2015. Usefulness of 3D surface roughness parameters for nondestructive evaluation of pull-off adhesion of concrete layers. Constr. Build. Mater. 84, 111–120.

Joanny, J.F., De Gennes, P.G., 1984. A model for contact angle hysteresis. J. Chem. Phys. 81 (1), 552–562.

Lago, M., Araujo, M., 2001. Threshold pressure in capillaries with polygonal cross-section. J. Colloid Interface Sci. 243, 219–226.

Liu, C., Liu, S., Wang, X., 2007. Numerical simulation and analysis of oil-water displacement behavior in rough capillary channel. Petrol. Geol. Exp. 29 (5), 522–526.

Lundgren, M., Allan, N.L., Cosgrove, T., 2007. Modeling of wetting: a study of nanowetting at rough and heterogeneous surfaces. Langmuir 23, 1187–1194.

Mason, G., Morrow, N.R., 1991. Capillary behavior of a perfectly wetting liquid in irregular triangular tubes. J. Colloid Interface Sci. 141, 262–274.

Martys, N.S., Chen, H., 1996. Simulation of multicomponent fluids in complex three-dimensional geometries by the Lattice Boltzmann method. Phys. Rev. E 53 (1), 743.

Mayer, R.P., Stowe, R.A., 1965. Mercury porosimetry—breakthrough pressure for penetration between packed spheres. J. Colloid Interface Sci. 20, 893–911.

Milne, A.J., Amirfazli, A., 2012. The cassie equation: how it is meant to be used. Adv. Colloid Interface Sci. 170 (1–2), 48.

Monfared, A.D., Ghazanfari, M.H., Jamialahmadi, M., Helalizadeh, A., 2015. Adsorption of silica nanoparticles onto calcite: equilibrium, kinetic, thermodynamic and DLVO analysis. Chem. Eng. J. 281, 334–344.

Morrow, N.R., 1975. The effects of surface roughness on contact: angle with special reference to petroleum recovery. J. Can. Petrol. Technol. 14 (4).

Mortazavi, V., D'Souza, R.M., Nosonovsky, M., 2013. Study of contact angle hysteresis using the Cellular Potts Model. Phys. Chem. Chem. Phys. 15, 2749–2756.

Oren, P.E., Bakke, S., Arntzen, O.J., 1998. Extending predictive capabilities to network models. SPE J. 3, 324–336.

Pan, C., Hilpert, M., Miller, C.T., 2004. Lattice-boltzmann simulation of two-phase flow in porous media. Water Resour. Res. 40 (1), 62–74.

Patzek, T., 2001. Verification of a complete pore network simulator of drainage and imbibition. SPE J. 6, 144–156.

Princen, H.M., 1969a. Capillary phenomena in assemblies of parallel cylinders: I. Capillary rise between two cylinders. J. Colloid Interface Sci. 30, 69–75.

Princen, H.M., 1969b. Capillary phenomena in assemblies of parallel cylinders: II. Capillary rise in systems with more than two cylinders. J. Colloid Interface Sci. 30, 359–371.

Princen, H.M., 1970. Capillary phenomena in assemblies of parallel cylinders: III. Liquid columns between horizontal parallel cylinders. J. Colloid Interface Sci. 34, 171–184.

Quéré, D., 2008. Wetting and roughness. Annu. Rev. Mater. Res. 38, 71–99.

Rao, Y., 2010. Nanofluids: stability, phase diagram, rheology and applications. Particuology 8, 549–555.

Rostami, A., Streator, J.L., 2017. A Model of capillary-driven flow between contacting rough surfaces. J. Tribol. 139 (3), 031401.

Shan, X., Chen, H., 1993. Lattice Boltzmann model for simulating flows with multiple phases and components. Phys. Rev. E 47 (3), 1815.

Shan, X., Chen, H., 1994. Simulation of nonideal gases and liquid-gas phase transitions by the Lattice Boltzmann equation. Phys. Rev. E 49 (4), 2941.

Sukop, M.C., Thorne, D.T., 2006. Lattice Boltzmann Modeling: An Introduction for Geoscientists and Engineers. Springer Publishing Company, Incorporated.

Tsakiroglou, C.D., Payatakes, A.C., 1993. Pore-wall roughness as a fractal surface and theoretical simulation of mercury intrusion/retraction in porous media. J. Colloid Interface Sci. 159, 287–301.

Tuller, M., Or, D., Dudley, L.M., 1999. Adsorption and capillary condensation in porous media: liquid retention and interfacial configurations in angular pores. Water Resour. Res. 35 (7), 1949–1964.

Verhulst, Pierre-François, 1845. Recherches mathématiques sur la loi d'accroissement de la population [Mathematical Researches into the Law of Population Growth Increase]. Nouveaux Mémoires de l'Académie Royale des Sciences et Belles-Lettres de Bruxelles 18, 1–42.

Wei, B., Hou, J., Zhou, K., Yu, B., 2015. Understanding the capillary behavior using the

extended reduced similar geometry method. Chem. Eng. Sci. 123, 420–428.

Wenzel, R.N., 1949. Surface roughness and contact angle. J. Phys. Colloid Chem. 53, 1466–1467.

Whyman, G., Bormashenko, E., Stein, T., 2008. The rigorous derivation of Young, Cassie-Baxter and Wenzel equations and the analysis of the contact angle hysteresis phenomenon. Chem. Phys. Lett. 450, 355–359.

Ye, Z., Liu, H.H., Jiang, Q., Liu, Y., Cheng, A., 2017. Two-phase flow properties in

aperture-based fractures under normal deformation conditions: analytical approach and numerical simulation. J. Hydrol. 545, 72–87.

Zhang, Cheng, Yu., Q., 2016. The effect of water saturation on methane breakthrough pressure: an experimental study on the Carboniferous shales from the eastern Qaidam Basin. China. J. Hydrol. 543, 832–848.

Zhang, Xiaoxian, Crawford, J.W., Young, I.M., 2016. A Lattice Boltzmann model for simulating water flow at pore scale in unsaturated soils. J. Hydrol. 538, 152–160.